Available online at www.sciencedirect.com
ScienceDirect
Applied Acoustics 69 (2008) 110–126
applied acoustics
www.elsevier.com/locate/apacoust

Computation of aeolian tone from a circular cylinder using source models

Cheolung Cheong [a,*], Phillip Joseph [b], Yonghwan Park [c], Soogab Lee [c]

[a] School of Mechanical Engineering, College of Engineering, Pusan National University, 30, Jangjeon-dong, Geumjeong-gu, Pusan 609-735, Republic of Korea
[b] Fluid Dynamics and Acoustics Group, Institute of Sound and Vibration Research, University of Southampton, Southampton SO17 1BJ, United Kingdom
[c] School of Mechanical and Aerospace Engineering, Seoul National University, Seoul 151-742, Republic of Korea

Received 11 May 2006; received in revised form 30 September 2006; accepted 12 October 2006
Available online 6 December 2006

Abstract

The generation of aeolian tones from a two-dimensional circular cylinder situated in a uniform cross-flow is investigated. The major emphasis here is placed on identifying the important noise generation mechanisms. Acoustic-viscous splitting techniques are utilized to compute modelled acoustic source terms and their corresponding acoustic fields. The incompressible Reynolds averaged Navier–Stokes equation is used to compute the near-field viscous flow solution, from which modelled acoustic source terms are extracted based on an approximation to the Lighthill's stress tensor. Acoustic fields are then computed with an acoustic solver to solve the linearized Euler equations forced by the modelled source terms. Computations of the acoustic field based on the approximated Lighthill's stress tensor are shown to be in good agreement with those computed from the surface dipole sources obtained using Curle's solution to the acoustic analogy. It is shown in this paper that the stress tensor source term in the streamwise direction makes a comparable, but slightly larger contribution to the overall radiated field, compared with that due to the stress tensor in the direction normal to the mean flow. In addition, it is shown that shear sources, which arise due to the interaction between the fluctuating velocity and the background steady mean velocity, make the greatest contribution to the acoustic field, while the self-noise sources, which represents the interaction between the fluctuating velocities, is shown to be comparably negligible.

Keywords: Aeolian tone; Lighthill's stress tensor; Shear-noise source; Self-noise source; Computational aeroacoustics

---

1. Introduction

Noise generated by a cylinder situated in a smooth cross-flow involves fundamental aeroacoustic noise generation mechanisms, which are known to be significant in airframe and power plant noise (tubular heat exchanger, power transmission lines, chimneys and airframe noise). This is one of reasons why aeolian tones generated by a steady flow over a circular cylinder have been one of most studied topics in aeroacoustics. The various studies on aeolian tone noise generation undertaken previously can be categorized into three groups according to the varying degree of complexity and accuracy of the noise prediction tools used.

The first group makes use of the semi-analytic methods. These involve separating the computation of the aerodynamic source term from that of the sound propagation. Computation of the sound propagation is based on integral formulas derived from the wave equations with source terms consisting of unsteady flow variables. Among the wave equation-type approaches, the most well-known is the wave equation formulated in Lighthill's acoustic analogy [1]. Lighthill's acoustic analogy has been extended by Curle [2] and by Ffowcs Williams and Hawkings [3] to allow for the effects of solid boundaries and their motion, respectively. In this first group of approaches, the source data is generated from techniques developed in computational

---

[*] Corresponding author. Tel.: +82 51 510 2311; fax: +82 51 514 7640.
E-mail address: ccheong@pusan.ac.kr (C. Cheong).

0003-682X/$ - see front matter © 2006 Elsevier Ltd. All rights reserved.
doi:10.1016/j.apacoust.2006.10.004

fluid dynamics (CFD). The works of Hardin et al. [4] and Cox et al. [5] fall into this group. This method is computationally more efficient compared with the other methods. However, most studies in this group have been dedicated to predicting aeolian tone noise from the point of view of Curle's acoustic analogy without consideration of the detailed noise generation mechanisms.

The second group is based on the hybrid numerical method where the flow quantities are represented by their "base flow" components plus their "residual" components, which leads to two separate sets of equations governing the viscous flow field and the acoustic disturbance field, respectively. The most significant advantage of the hybrid numerical method is that numerical algorithms are used that are most suitable to the solver of the viscous flow field and the acoustic field. The hybrid numerical method for low-speed aeroacoustics, so-called the expansion about incompressible flow (EIF) method, is mainly due to Hardin and Pope [6,7]. Their method utilizes prediction of the entire incompressible viscous flow field, which is obtained from the incompressible Navier–Stokes equations. Once a correction to the constant hydrodynamic density is obtained, acoustic radiation can be predicted from the compressible Euler equations in which the dependent variables are split into hydrodynamic terms and the acoustic terms. Shen and Sørensen [8] found inconsistencies in this formulation and proposed modification to overcome it. This new formulation was applied to laminar flows around a circular cylinder [9] and turbulent flows past an airfoil [10]. Another numerical hybrid method is based on the acoustic perturbation equations of Ewert and Schröder [11]. These equations are driven by the source terms determined from a prediction of the compressible or incompressible flow. They applied this method to a laminar flow over a cylinder. However, the results obtained in this group were qualitative, and detailed descriptions of the acoustic field and its generation mechanism were not provided.

The third group of investigations into aeolian tone generation makes use of computation aeroacoustics (CAA) techniques which use the unsteady compressible Navier–Stokes equations to directly calculate the acoustic field. Recent major developments in the understanding of aerodynamic noise generation mechanisms were based on CAA. However, it is still difficult to perform a direct computation of the aerodynamic noise due to the immense computational resources and high cost required in solving low-Mach number aeroacoustic problems. Most works for low-Mach number aeroacoustics is therefore confined to laminar flows. Recently, Inoue and Hatakeyam [12] made use of direct numerical simulation (DNS) to investigate aeolian tone noise radiation due to a two-dimensional circular cylinder in a laminar cross-flow at low-Mach number. Through the comparison of the results of the DNS with the solutions obtained using Curle's acoustic analogy, they showed that Curle's solution, including Doppler effects, accurately describes, not only the generation mechanism of the sound, but also the propagation process. However, their results seem to be inadequate in showing the detailed mechanism of aeolian tone noise generation. This is partially due to the intrinsic difficulty of DNS in assessing the relative contributions of the noise sources since individual sources cannot be distinguished.

Although there have been many studies on aeolian tone generation from a circular cylinder, as described above, most of this work is from the point of view of Curle's acoustic analogy, whose interpretation is that the unsteady surface dipole sources due to unsteady pressure over the surface of the cylinder make most contribution to aeolian tone radiation. Whilst the Curle's formulation is useful in predicting the far-field acoustic pressure effectively, it does not provide a clear strategy for modifying the acoustic sources and hence reducing the corresponding tone. The dipole source distribution due to the unsteady loading of a body in a flow is simply a reaction to the force exerted by fluid on the body. In this respect, the dipole source can be considered as an essentially passive source. In order to provide a basic philosophy for the low-noise design, the detailed source mechanism must be identified. This is the main motivation behind the work presented in this paper.

In this paper, aeolian tone produced by a two-dimensional circular cylinder in a uniform cross-flow is investigated with emphasis placed on its tone generation mechanisms by the use of the hybrid CAA method. Firstly, the incompressible Navier–Stokes equations are solved using conventional CFD techniques. The linearized Euler equations are then solved using high-order CAA techniques with modelled source terms deduced from the approximated Lighthill's stress tensor using the unsteady flow simulation determined from the CFD calculation. The hybrid CAA method used is based on the assumption that acoustic wave propagation is essentially inviscid in nature and that acoustic pressure perturbations are so small that their contribution to the flow convection velocity is negligible. Viscous effects are generally negligible in a sound field because the acoustic Reynolds number, $Re_{\mathrm{a}} = 2\pi c\lambda/v$ (c is the speed of sound, λ is the wavelength, v is the kinematic viscosity), representing the ratio of the pressure stress to the viscous stress, is usually very large, being of the order of 10^8 at the most audible frequencies [13]. However, the flow Reynolds number, $Re_{\mathrm{f}} = u_\infty D/v$ (u_∞ is mean-flow velocity and D is the diameter of a circular cylinder), representing the ratio of inertia force to viscous force, is an important factor to determine the dynamics of flow in the source region; laminar, transition and turbulent flows. It is well known that the flow patterns around a circular cylinder vary depending on the Reynolds number. Using the Strouhal number, $St = D/\lambda M$ (M is the Mach number), the relation between the acoustic and the flow Reynolds numbers may be derived of the form, $Re_{\mathrm{a}} = 2\pi S_{\mathrm{t}}/M^2 \cdot Re_{\mathrm{f}}$ which shows that the acoustic Reynolds number is M^{-2} times larger than the flow Reynolds number. Furthermore, the acoustic length-scale is typically M^{-1} times longer than the flow length-scale. The hybrid techniques using the separate solvers for viscous source field and inviscid sound field accommodate this Reynolds number difference and disparate length-scales associated with low Mach number aeroacoustics. The convective length-scales can be resolved on a hydrodynamic grid, while the acoustic length-scales can be resolved on a separate acoustic grid. The validity of this hybrid approach was verified by comparing the numerical solution with the analytic solution of the sound field due to a two-dimensional point dipole whose source strength is computed from the lift and dipole coefficients. To investigate the tone generation mechanism in detail, acoustic simulations are performed by splitting the approximated Lighthill stress tensor into its various components, each of which can be associated with a distinct tone generation mechanism.

The main contribution of this paper is to clarify the source mechanisms which play an important role in generating aeolian tone from the point of view of Lighthill's acoustic analogy rather than Curle's acoustic analogy, which interprets the aerodynamic sources as surface sources. Clarification of the main source mechanism in terms of the Lighthill stress tensor distribution provides a framework for the low-noise design of practical wall-bounded sheared flow problems such as valve noise [14].

This paper is organized into five sections. Section 2 presents the fundamental equations for predicting the modelled aerodynamic source terms. The incompressible Navier–Stokes equations with the k–ε turbulence closure model for viscous flow fields are also reviewed. In Section 3, the numerical methods are presented for solving the acoustic and flow fields. In Section 4, aeolian tone noise due to a cross-flow past a circular cylinder is investigated using the numerical methods described in Section 3. Conclusions from this work are presented in the last section.

2. Fundamental equations

Lighthill [3] rearranged the continuity equation and the Navier–Stokes equation into a single equation whose left-hand side is the acoustic wave operator of the form

$$\frac{\partial^2 \rho'}{\partial t^2} - c^2 \frac{\partial^2 \rho'}{\partial x_i \partial x_i} = -\frac{\partial S_i}{\partial x_i}. \tag{1}$$

On the right-hand side of Eq. (1), $S_i = -\partial T_{ij}/\partial x_j$ where T_{ij} denotes the Lighthill stress tensor defined by $T_{ij} = \rho u_i u_j + (p' - c^2\rho')\delta_{ij} - \tau_{ij}$, where τ_{ij} is the viscous stress tensor. In order to utilize the CAA techniques for solving Eq. (1), it is decomposed into the linearized mass and momentum continuity equations together with the isentropic relation $p' = c^2\rho'$, as follows:

$$\frac{\partial \rho'}{\partial t} + \rho_0 \frac{\partial u_i}{\partial x_i} = 0, \tag{2}$$

$$\rho_0 \frac{\partial u_i}{\partial t} + \frac{\partial p'}{\partial x_i} = S_i, \tag{3}$$

$$\frac{\partial p'}{\partial t} + \rho_0 c^2 \frac{\partial u_i}{\partial x_i} = 0. \tag{4}$$

Note that Eqs. (2)–(4) are similar to those of the linearized Euler equations with modelled source terms, but do not include the interaction terms between the acoustical and mean flow quantities. Eqs. (2)–(4) are used as the equations governing the behavior of the acoustic field. Assuming that the viscous stress and the entropy fluctuations are negligible within the moving fluid, the acoustic source terms S_i are modelled using the approximated Lighthill's stress tensor (ALST), as follows:

$$S_i = S_{\mathrm{ALST},i} = -\frac{\partial \rho u_i u_j}{\partial x_j}. \tag{5}$$

Decomposing the velocity into mean and fluctuating parts gives

$$S_{\mathrm{ALST},i} = -\frac{\partial \rho (u_i' + \bar{u}_i)(u_j' + \bar{u}_j)}{\partial x_j}, \tag{6}$$

which may be expanded as

$$S_{\mathrm{ALST},i} = -\frac{\partial \rho u_i' u_j'}{\partial x_j} - \frac{\partial \rho u_i' \bar{u}_j}{\partial x_j} - \frac{\partial \rho \bar{u}_i u_j'}{\partial x_j} - \frac{\partial \rho \bar{u}_i \bar{u}_j}{\partial x_j}. \tag{7}$$

Eq. (7) may be grouped into the three separate terms:

$$S_{\mathrm{ALST},i} = S_{\mathrm{self},i} + S_{\mathrm{shear},i} + S_{0,i}, \tag{8}$$

the first two of which may be associated with a distinct sound generating mechanism. They are given by

$$S_{\mathrm{self},i} = -\frac{\partial \rho u_i' u_j'}{\partial x_j}, \tag{9}$$

$$S_{\mathrm{shear},i} = -\frac{\partial \rho u_i' \bar{u}_j}{\partial x_j} - \frac{\partial \rho \bar{u}_i u_j'}{\partial x_j}. \tag{10}$$

The third term is of the form

$$S_{0,i} = -\frac{\partial \rho \bar{u}_i \bar{u}_j}{\partial x_j}. \tag{11}$$

Here, $u_i'(\mathbf{x}, t) = u_i(\mathbf{x}, t) - \bar{u}_i(\mathbf{x})$ denotes the fluctuating velocity component and $\bar{u}_i(\mathbf{x}) = \lim_{T\to\infty} \frac{1}{T}\int_0^T u_i(\mathbf{x}, t)\mathrm{d}t$ denotes the steady velocity component. The first term $S_{\mathrm{self},i}$ on the right-hand side of Eq. (8) denotes the self-noise source term corresponding to the interaction between fluctuating velocities. The second term $S_{\mathrm{shear},i}$ represents the shear-noise source terms that accounts for the interaction between the fluctuating velocity and the mean velocity. The last term $S_{0,i}$ consists entirely of steady terms and thus does not constitute an acoustic source. Note that the quadrupole source model (QSM) by Bogey et al. [15],

$$S_{\mathrm{QSM},i} = -\left(\frac{\partial \rho u_i' u_j'}{\partial x_j} - \frac{\overline{\partial \rho u_i' u_j'}}{\partial x_j}\right), \tag{12}$$

is equivalent to the self-noise source in Eq. (8) with mean value subtracted. They showed that this source model is the most appropriate for sound generated in free sheared flows. One of the main objective of the present paper is to establish the relative importance of shear-noise sources and self-noise sources to aeolian tone generation, which may differ substantially from the sound generation by free sheared flows.

The source terms of Eqs. (5), (9) and (10) were computed using the 2-D incompressible Reynolds-averaged Navier–Stokes (RANS) equations for viscous flows. Compressibility effects due the interactions between the acoustical and mean-flow velocities, and between the acoustical and vortical velocities, are therefore absent from the source terms. The incompressible RANS equations may be summarised thus:

$$\frac{\partial u_i}{\partial x_i} = 0, \tag{13}$$

$$\frac{\partial u_i}{\partial t} + u_j \frac{\partial u_i}{\partial x_j} = -\frac{1}{\rho}\frac{\partial p}{\partial x_i} + v_{\text{eff}} \frac{\partial^2 u_i}{\partial x_j^2}, \tag{14}$$

where v_{eff} is the effective viscosity defined as $v_{\text{eff}} = v + v_{\text{t}}$, and the eddy viscosity v_{t} is modelled using the low Reynolds number k–ε turbulence model by Chien [16]. The eddy viscosity v_{t} is given by

$$v_{\text{t}} = C_\mu f_\mu \frac{k^2}{\varepsilon}, \tag{15}$$

where k is the turbulent kinetic energy, ε is the turbulence energy dissipation and f_μ is defined as $f_\mu = 1 - \mathrm{e}^{-0.0115 u_* y/v}$ where u_* is the friction velocity and y is the normal distance from the wall. Two equations are involved in this turbulence model; one for the turbulence kinetic energy k and the other for the turbulence energy dissipation ε, as follows:

$$\frac{\partial k}{\partial t} + \frac{\partial u_j k}{\partial x_j} = \frac{1}{\rho}\frac{\partial}{\partial x_j}\left[\left(\mu + \frac{\mu_{\text{t}}}{\sigma_k}\right)\frac{\partial k}{\partial x_j}\right] + \mu_{\text{t}}\left(\frac{\partial u_i}{\partial x_j} + \frac{\partial u_j}{\partial x_i}\right)\frac{\partial u_j}{\partial x_i} - k\left(f_\mu C_\mu \rho \frac{k}{\mu_{\text{t}}} + \frac{2\mu}{y^2}\right), \tag{16}$$

$$\frac{\partial \varepsilon}{\partial t} + \frac{\partial u_j \varepsilon}{\partial x_j} = \frac{1}{\rho}\frac{\partial}{\partial x_j}\left[\left(\mu + \frac{\mu_{\text{t}}}{\sigma_\varepsilon}\right)\frac{\partial k}{\partial x_j}\right] + f_1 C_{\varepsilon 1} \mu_{\text{t}}\left(\frac{\partial u_i}{\partial x_j} + \frac{\partial u_j}{\partial x_i}\right)\frac{\partial u_j}{\partial x_i} - C_{\varepsilon 2} f_2 \frac{\varepsilon^2}{k} - 2\varepsilon v \frac{\mathrm{e}^{-0.5 u_* y/v}}{y^2}. \tag{17}$$

The empirical low-Reynolds number functions f_μ, f_1 and f_2 appearing in the ε-equation (17) are given by

$$f_1 = 1.0, \quad f_2 = 1 - 0.22\exp[-(R_T/6)^2], \tag{18}$$

where $R_{\text{T}} = k^2/v\varepsilon$. The remaining empirical constants were allocated the following standard values cited by Chien: $C_\mu = 0.09$, $C_{\varepsilon 1} = 1.35$, $C_{\varepsilon 2} = 1.80$, $\sigma_k = 1.0$, and $\sigma_\varepsilon = 1.30$.

Solving the RANS with a time-accurate integration method is sometimes referred to as a VLES (very large eddy simulation). As Shen and Sørensen [10] have indicated, the reason for choosing Reynolds averaging instead of LES filtering is due to the fact that LES filtering in a two-dimensional problem introduces non-physical solutions such as inverse cascade phenomena for the higher frequency in the inertial subrange.

3. Numerical methods

3.1. Numerical methods for computational aeroacoustics

The Cartesian coordinate system employed in Eqs. (2)–(4) is inconvenient for solving problems which include curvilinear boundary lines. Thus, the spatial derivatives expressed as functions of the coordinates (x_1, x_2) need to be recast as functions of the curvilinear coordinates (ξ, η) by a general coordinate transformation. All variables are then non-dimensionalized with the following scales: D (cylinder diameter) for the length scale, c_∞ for the velocity scale, D/c_∞ for the time scale, ρ_∞ for the density scale and $\rho_\infty c_\infty^2$ for the pressure scale, where c_∞ is the ambient speed of sound. The seven-point stencil, grid-optimized dispersion-relation-preserving (GODRP) scheme of Cheong and Lee [17] was utilized to compute the spatial flux derivatives. Tam and Webb [18] have shown, that if a given numerical scheme and the governing equations share the same dispersion relation, the numerical and exact solutions will have the same wave propagation characteristics and wave speeds. Accordingly, they developed the classic dispersion-relation-preserving (DRP) scheme, which essentially preserves the wave propagation characteristics of the governing equations. The DRP scheme is usually implemented on a uniform Cartesian grid. However, actual problems in aeroacoustics are seldom this regular, with the associated computational grids usually being non-uniform or curvilinear. Thus, the GODRP schemes were developed with the grid-optimization algorithm so that the finite difference equations will have the same dispersion relations as the corresponding partial differential equations for general geometries, including non-uniform Cartesian or curvilinear grids. A detailed description of the GODRP scheme is given in Ref. [17]. Time integration is performed with the low-dissipation and low-dispersion Runge–Kutta schemes introduced by Hu et al. [19] which minimises dissipation and dispersion wave propagation errors. The transfer of flow information across the out-flow boundaries of the computational domain is associated with acoustic waves, vorticity waves and entropy waves. The radiation and outflow boundary conditions [18,20], based on the asymptotic expressions for the three characteristic waves of Euler's equations in the far field, are implemented across the out-flow boundaries. For inviscid flows, the well-known boundary condition at a solid wall is that the velocity component normal to the wall must be equal to zero. This condition is sufficient to determine a unique solution to the Euler equations. For a high-order finite difference scheme the order of the difference equations is higher than that of the Euler equations. Thus, the zero normal velocity boundary condition is insufficient for determining a unique solution. Therefore, additional numerical constraints must be imposed. Here, the ghost value of pressure [21] was used as the extraneous boundary condition. Physically the wall exerts a pressure on the fluid with a magnitude just enough to make the normal velocity zero at its surface. This suggests that a ghost value in pressure at the ghost point immediately below the wall should be used to simulate the pressure of the wall. The ghost value of pressure at the ghost point of nth time step is to be chosen so that the velocity normal to the wall of nth time step is zero by using the momentum equations. Then the computed ghost value of pressure is used to compute the other dependent variables at the $(n+1)$th time step. In some cases, it is necessary to remove spurious numerical oscillations. The artificial selective damping technique of Tam and Shen [22] was used to suppress such spurious waves.

3.2. Numerical methods for viscous flow simulations

The numerical method used for performing the viscous flow field prediction is based on the unstructured grid, finite-volume method, presented in detail by Kang et al. [23,24]. The scheme has extended the unstructured grid Navier–Stokes procedure of Thomadakis et al. [25] for incompressible flows to allow the collocated storage of all variables. Since Thomadakis et al. used a staggered-grid formulation, pressure data could be stored at the centroid of a cell while velocity components were stored at grid points. However, the scheme has been modified so that this procedure can employ collocated storage (non-staggered) to obviate the difficulties and disadvantages of implementing a non-collocated (staggered) mesh within the unstructured methodology.

The algebraic equation for hydrodynamic pressure was derived by substituting the discretized momentum equations into the continuity equation [26]. The process of deriving the pressure equation is almost the same as that used for the structured grid method. To retain second-order accuracy of space and time discretization, the numerical method uses the quadratic upstream interpolation for convective kinematics (QUICK) scheme for the convective terms and the second-order Euler backward difference scheme for computing the time derivatives. All other spatial derivatives are approximated by the central difference schemes.

4. Numerical results

The numerical procedure outlined above for predicting the generation and propagation of aeolian tone noise is summarised in Fig. 1.

One of the advantages of the current approach is that it is able to capture disparate length scales linked with low-Mach number flow-induced noise, where the acoustic wavelength is typically M^{-1} times longer than the flow length scale. The smaller convective length scales are resolved on an aerodynamic grid, while the acoustic length scales are resolved on a separate acoustic grid. Accordingly, the computed acoustic source data must be transformed from the grid and time-steps used for the flow-simulation into the grid and time-steps used for the acoustic simulation. The strategy used to perform this transformation is to construct the acoustic source terms with their associated gradients on the grid and time-steps for the flow simulation and interpolate their values onto the grid and time step for the acoustic simulation. This reduces the discretization error relative to the alternative approach of interpolating the incompressible flow primitive variables onto the acoustic grid and computing the source terms using the same level of discretization provided by the acoustic grid spacing.

The numerical approach described above was applied to the prediction of aeolian tone noise due to flow over a two-dimensional cylinder. The Reynolds number of the problem, defined as $Re = u_{\infty}D/\nu$, is equal to 1.58×10^4. The circular

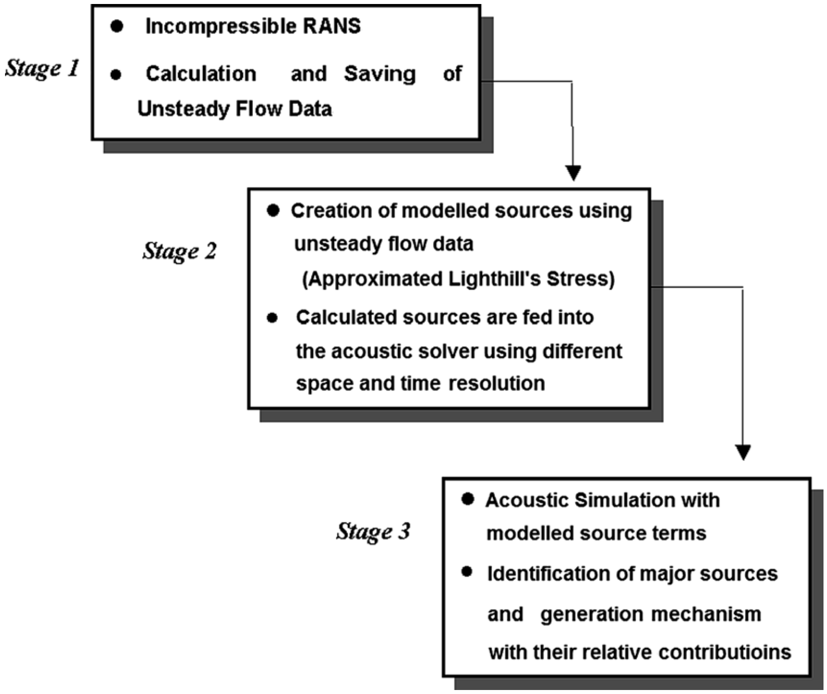

Fig. 1. Numerical procedure for current computations.

cylinder diameter and the uniform upstream velocity are 9.55 mm, and 24.5 m/s, respectively. These conditions were chosen to meet the general flow conditions in typical tubular heat exchangers and to coincide with existing experimental data of the flow dynamics presented by Kiya et al. [27] and Cantwell and Coles [28].

4.1. Numerical results of the viscous flow simulation

The size of the computational domain and the boundary conditions applied in the simulation are shown in Fig. 2. The computational domain used was $-10D \leqslant x_1 \leqslant 20D$ and $-10D \leqslant x_2 \leqslant 10D$ where x_1 is the coordinate in the streamwise direction. The origin of the Cartesian coordinate system corresponds to the center of the cylinder. Dirichlet boundary conditions were used at the far field boundaries as well as at the cylinder surface. The convective boundary conditions, $\partial u/\partial t + c\partial u/\partial x_1 = 0$ and $\partial v/\partial t + c\partial v/\partial x_1 = 0$ were used as the outflow boundary condition in order to smoothly pass vorticity waves from the computational domain. In addition to the initial flow condition and the boundary conditions for the velocity, the free stream inlet turbulence values for the kinetic energy $k = 3/2(I_u u_\infty)^2$ and the turbulence dissipation $\varepsilon = 10C_\mu k^{3/2}/L_x$ have been imposed corresponding to a turbulence intensity (I_u) of 0.6% and a non-dimensional turbulence length scale (L_x/D) of 0.02 for the k–ε based turbulence model.

The flow calculations were carried out on a mesh with approximately 20,000 grid points. The mesh, and a close-up around the cylinder, are shown in Fig. 3. The mesh for performing viscous flow simulation consists of two grid types: an inner mesh consisting of a multiply connected grid and an outer Cartesian grid. The inner mesh size was increased according to the distance from the cylinder surface, and the distance of the first grid point from the cylinder surface was chosen to be 0.04% of the cylinder diameter (of the order of $\Delta x^+ = 1$) to ensure adequate spatial resolution in the laminar sub-layer. Initially, random disturbances were imposed on the uniform velocity field to ensure that vortex shedding occurs quickly. The computational time step was fixed as $\Delta t = 0.01 \cdot (D/u_\infty)$.

Fig. 4 shows the iso-contours of pressure and vorticity at a non-dimensional time of $t_f = 201.4$. Alternating vortex shedding can be observed behind the cylinder. Lift and drag forces exerted on the cylinder surface fluctuate in time

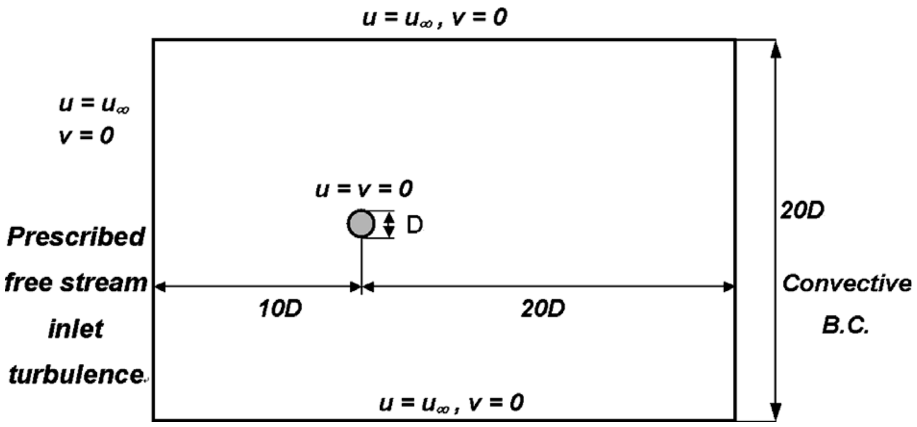

Fig. 2. Computation domain and applied boundary conditions for the incompressible flow simulation of the cross-flow over a circular cylinder.

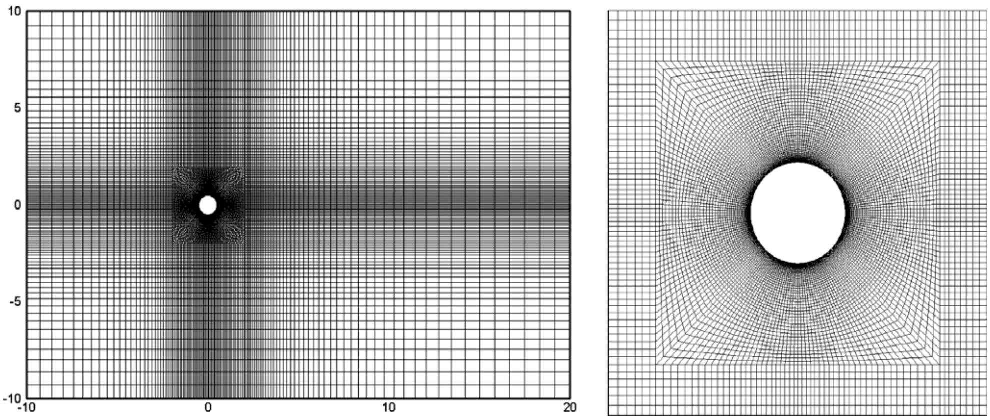

Fig. 3. The computational mesh used for the viscous flow simulation. (left: global domain mesh, and right: its close-up around the cylinder).

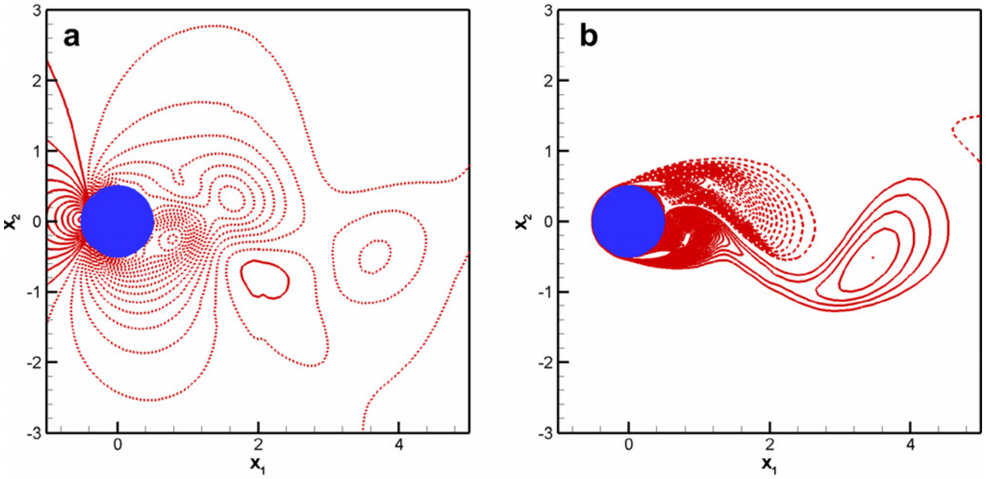

Fig. 4. Non-dimensional pressure, $(p - p_\infty)/p_\infty u_\infty^2$, and vorticity contours at non-dimensional time $t_f = 201.4$; (a) pressure contours from -1 to 0.5 with an increment of 0.05 and (b) vorticity contours from -7 to 7 with an increment 0.25; negative lines are denoted by the dashed lines.

due to the periodic shedding of vortices. The frequency of the vortex shedding can be estimated by evaluating the periodicity of the oscillating lift or drag coefficient.

Time-dependent lift and drag coefficients are presented in Fig. 5, calculated by integrating the distributions of pressure and shear stresses on the cylinder surface. Although the computation begins from an initial condition with randomly imposed disturbances, vortex shedding does not occur until a non-dimensional time $t_f = 180$. However, once the first shedding occurs, the flow solution passes through a transient interval to reach steady state where vortices are shed periodically. Lift and drag coefficients exhibit a sinusoidal time variation corresponding to a Strouhal number of 0.192 and 0.384, respectively. These values are in good agreement with experimental measurement [27]. It is noted that the drag oscillate at twice the Strouhal number corresponding to the fluctuating lift.

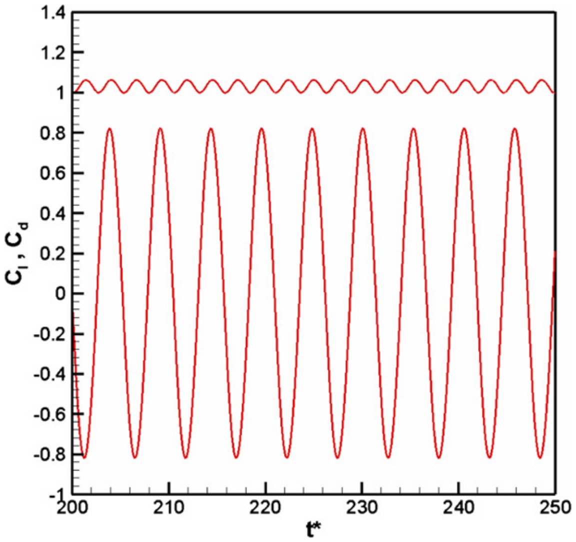

Fig. 5. Time-dependent signals of lift and drag coefficients.

Fig. 6 shows a comparison between the measured and predicted time-averaged drag coefficient and vortex-shedding Strouhal number. Reasonable agreement is observed at the Reynolds number $Re = 1.58 \times 10^4$ of the simulation. The upper and lower curves in Fig. 6 represent the variability in the experimental data collected by Cantwell and Coles [28]. The amplitude of the fluctuating lift is approximately ten times greater than that of the fluctuating drag. Thus, if the Curle's acoustic analogy were applied to this problem under the assumption of compact sources, the magnitude of the lift dipole sources would be predicted to be ten times greater than that of the drag dipole sources.

4.2. Transformation of flow data for use with the CAA solver

Hydrodynamic unsteady data obtained from the viscous flow simulation using the incompressible RANS solution are now used to compute the acoustic source terms in Eq. (3). The modelled source terms of Eqs. (5), (9) and (10) were computed at every iteration within a single vortex shedding period over the full flow computation domain. The non-dimensional period T_f of the vortex shedding is equal to 5.2 with $\Delta t_f = 0.01$ and the full computation domain is a square domain of size $[(-10D, 20D), (-10D, 20D)]$. These correspond to 520 data points in time and 20,000 grid points in space, respectively. Physical time was non-dimensionalized by D/u_∞ in the viscous flow simulation, and by D/c_∞ in the acoustic simulation. The different time-scales in the acoustic simulation and the viscous flow simulation leads to the different non-dimension period of $T_a = 72.25$ in the acoustic simulations (subscript a means the quantity related to the acoustic simulations). The numerical time step, Δt_a, used for the acoustic simulations is set to be 0.02, i.e., 3614 data points to represent one period of oscillation. Furthermore, the mesh for the acoustic calculation is the O-type grid which extends to the far-field reaching to $100D$ in this computation. Thus, the domain includes both the near field and the far field. The

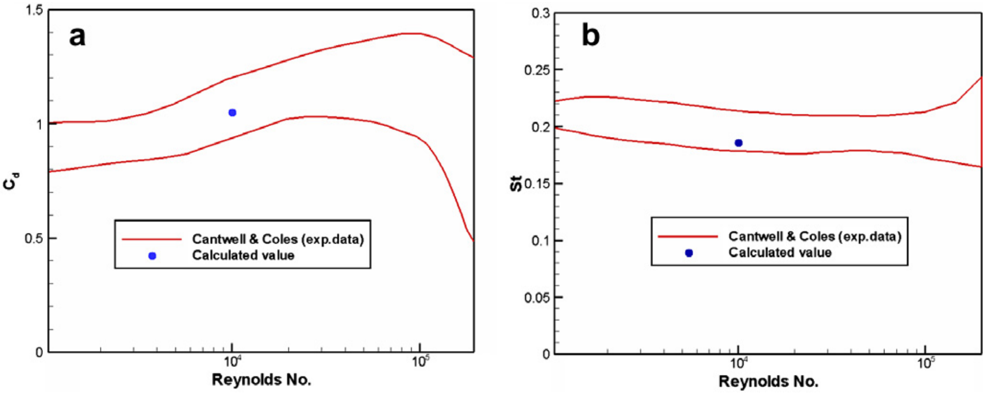

Fig. 6. Comparisons of the time-averaged drag coefficient $\overline{C}_d$ and the vortex-shedding Strouhal number S_t of the numerical result with experimental data; (a) $\overline{C}_d$ vs. *Re* and (b) S_t vs. *Re*.

calculated quadrupole source terms of Eqs. (5), (9) and (10) were transformed onto the grid and the time steps for acoustic simulation.

The acoustic source terms of Eqs. (5), (9) and (10), predicted using this procedure, are shown in Figs. 7–9, respectively. The predicted results of the approximated Lighthill's stress tensor (ALST) of Eq. (5) are shown in Fig. 7, while Fig. 7a and b shows the distribution of the $S_{\mathrm{ALST},1}$ term at approximately $0.25T_a$ and $0.75T_a$, respectively. Here, $0.25T_a$ corresponds to the time of minimum lift coefficient during one period of vortex shedding in Fig. 5 and therefore $0.75T_a$ denotes the time of maximum lift coefficient. Fig. 7c and d shows the distribution of the $S_{\mathrm{ALST},2}$ term at approximately $0.25T_a$ and $0.75T_a$, respectively. The magnitude of the fluctuating stress tensor in the x_1-direction is comparable to, but slightly larger than, that in the x_2-direction. Considering only the quantitative contributions of the acoustic sources, it can be expected that the

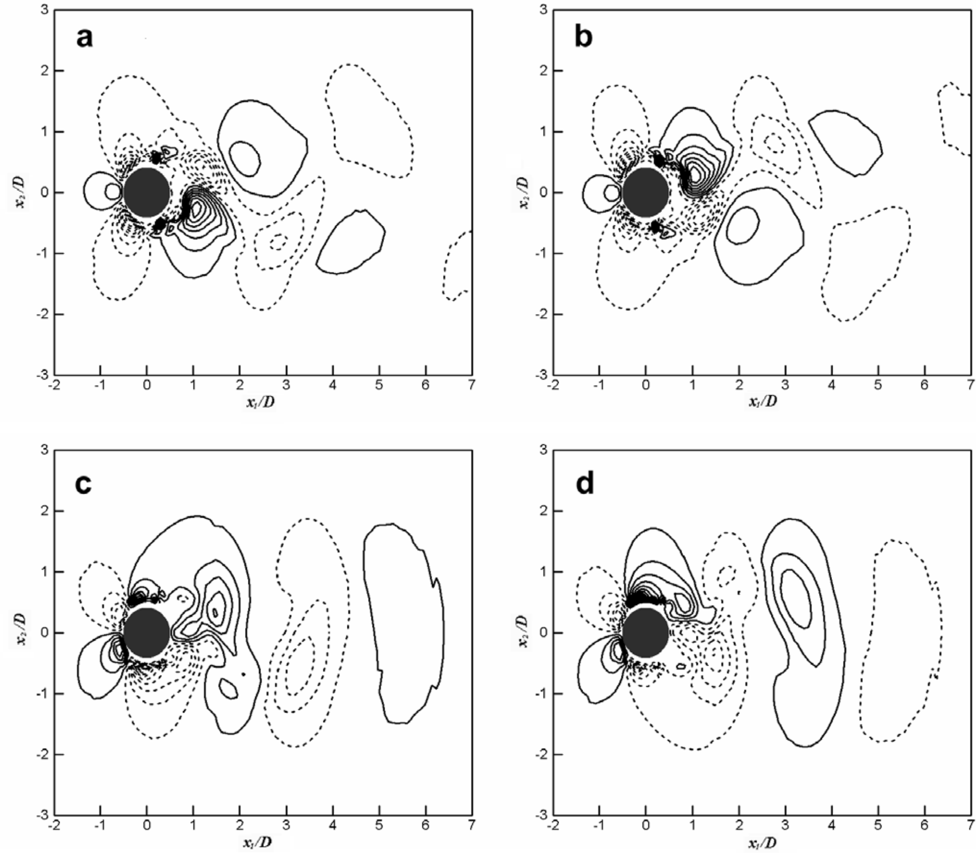

Fig. 7. Representation of the approximated lighthill stress tensor (ALST) source terms of Eq. (5); —, positive values and ---, negative values: (a) and (b) show the normalized $S_{\mathrm{ALST},1}$ with 20 contours from −1e−2 to 1.6e−2 at $0.25T_a$ and at $0.75T_a$, respectively, and (c) and (d) show normalized $S_{\mathrm{ALST},2}$ with 20 contours from −1.1e−2 to 1.1e−2 at $0.25T_a$ and $0.75T_a$, respectively.

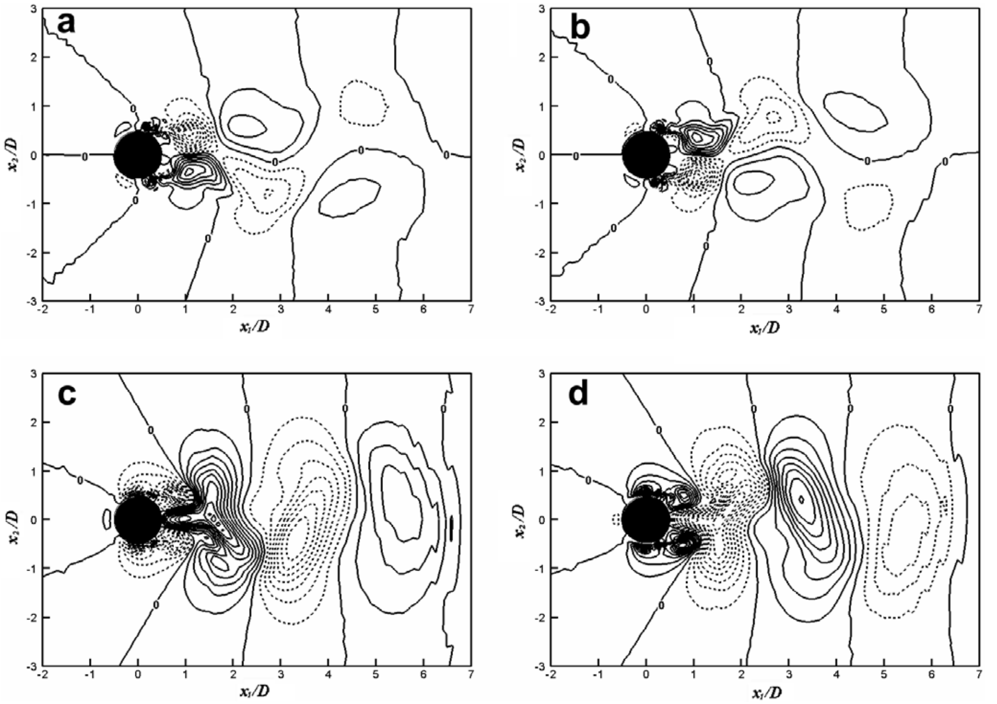

Fig. 8. Representation of the shear-noise source terms of Eq. (10); —, positive values, ---, negative values, and zero contour is denoted by 0: (a) and (b) show normalized $S_{\mathrm{shear},1}$ with 23 contours from −1.1e−2 to 1.1e−2 at $0.25T_\mathrm{a}$ and at $0.75T_\mathrm{a}$, respectively, and (c) and (d) show normalized $S_{\mathrm{shear},2}$ with 21 contours from −0.4e−2 to 0.4e−2 at $0.25T_\mathrm{a}$ and $0.75T_\mathrm{a}$, respectively.

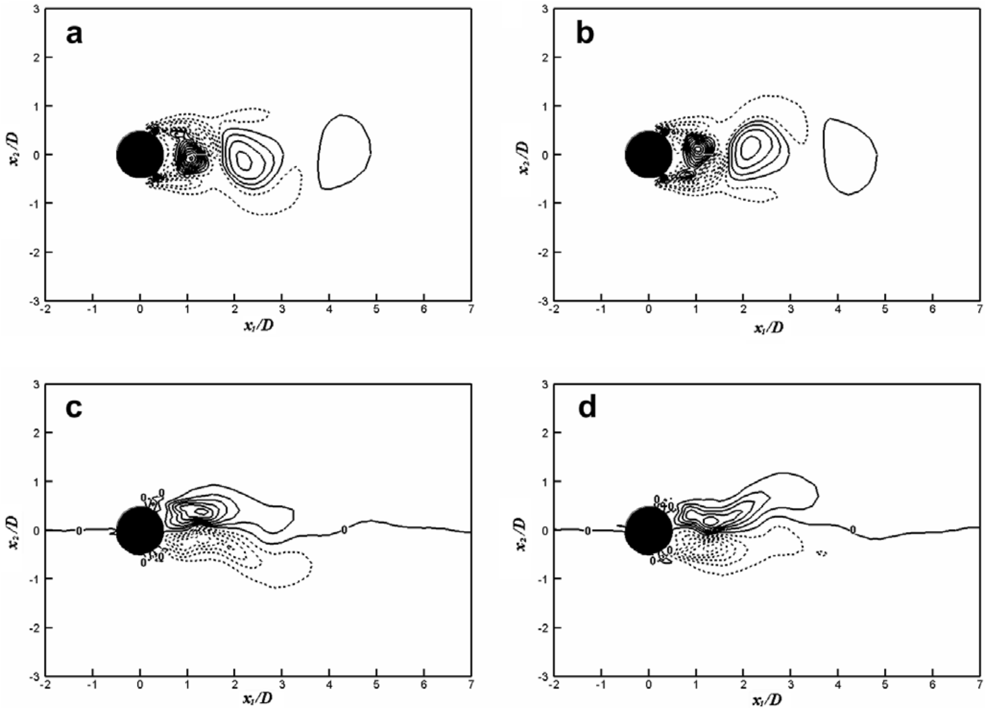

Fig. 9. Representation of the self-noise source terms of Eq. (9); —, positive values, and ---, negative values: (a) and (b) show normalized $S_{\mathrm{self},1}$ with 20 contours from −0.4e−2 to 0.6e−2 at $0.25T_\mathrm{a}$ and at $0.75T_\mathrm{a}$, respectively, and (c) and (d) show normalized $S_{\mathrm{self},2}$ with 19 contours from −0.45e−2 to 0.45e−2 at $0.25T_\mathrm{a}$ and $0.75T_\mathrm{a}$, respectively.

contribution from $S_{\mathrm{ALST},1}$ to total aeolian tone noise is also comparable to, but slightly larger, than that due to $S_{\mathrm{ASLT},2}$. This relative contribution is investigated in detail in Section 4.3. Fig. 8 shows the predicted spatial distribution of the shear-noise sources of Eq. (10). Fig. 8a and b shows the distribution of the $S_{\mathrm{shear},1}$ term at approximately $0.25T_\mathrm{a}$ and

$0.75T_a$, respectively. Fig. 8c and d shows the distribution of the $S_{\mathrm{shear},2}$ term at approximately $0.25T_a$ and $0.75T_a$, respectively. The magnitude of the fluctuating shear-noise source terms in the x_1-direction is observed to be larger than that in the x_2-direction.

Fig. 9 shows contours of the fluctuating self-noise source terms of Eq. (9). Fig. 9a and b shows the distribution of the $S_{\mathrm{self},1}$ term at approximately $0.25T_a$ and $0.75T_a$, respectively. Fig. 9c and d shows the distribution of the $S_{\mathrm{self},2}$ term at approximately $0.25T_a$ and $0.75T_a$, respectively. The frequency of oscillation of the self-noise source in the x_1-direction is found to be approximately twice that in the x_2-direction.

For a clearer view of this feature, Fig. 10a–f shows the self-noise source with its mean value subtracted and is thus equivalent to the source term defined by Bogey et al. [15] in

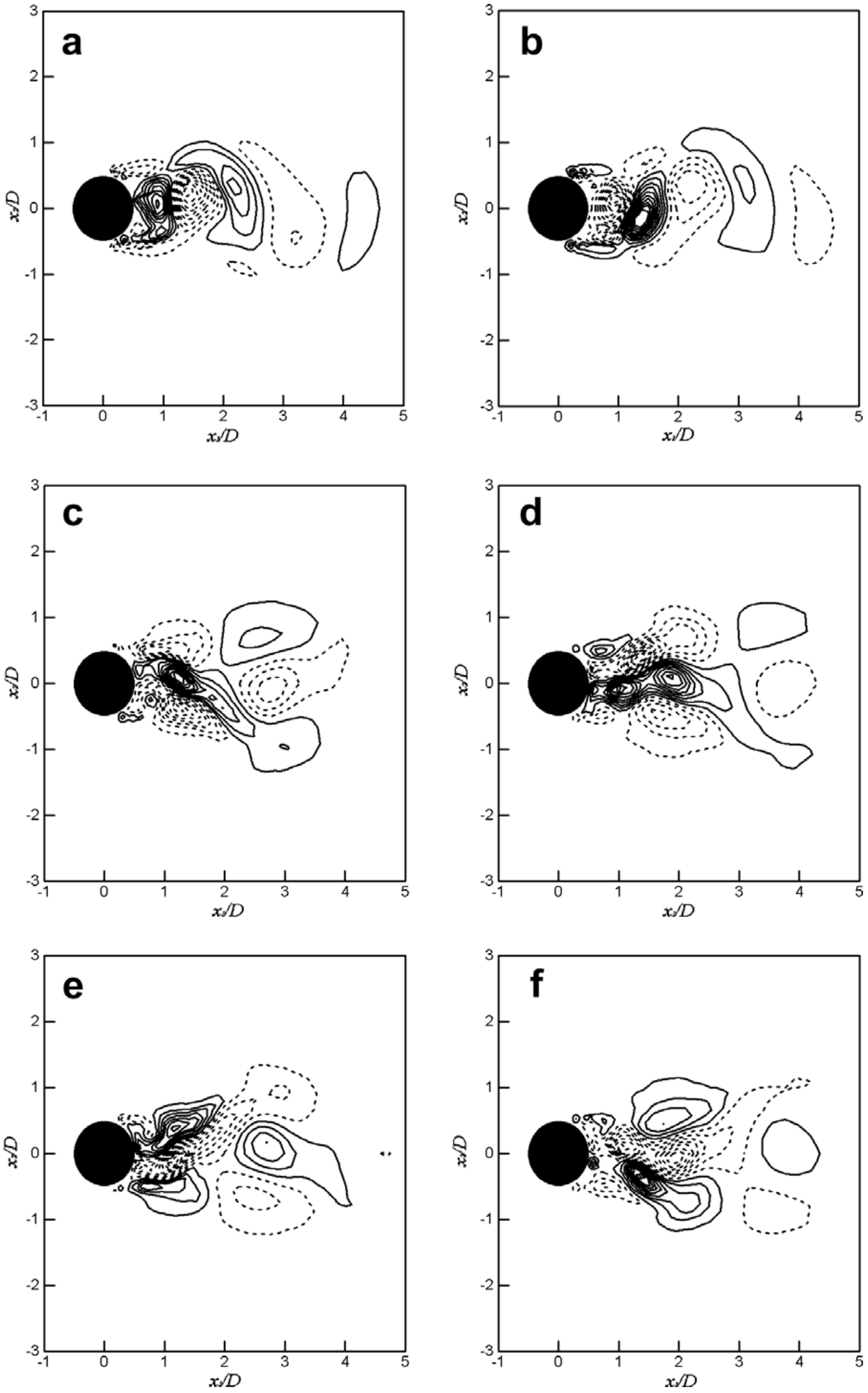

Fig. 10. Representation of the source terms of Eq. (12); —, positive values and - - -, negative values: (a) and (b) show normalized $S_{\mathrm{QSM},1}$ with 20 contours from −4e−3 to 4e−3 at $0.5T_a$and at $0.75T_a$, respectively. (c)–(f) show normalized $S_{\mathrm{QSM},2}$ with 15 contours from −1.9e−3 to 1.9e−3 at 0, $0.25T_a$, $0.5T_a$ and $0.75T_a$, respectively.

Eq. (12). Fig. 10a and b shows the distribution of the $S_{\mathrm{QSM},1}$ term of Eq. (12) at approximately $0.5T_{\mathrm{a}}$ and $0.75T_{\mathrm{a}}$, respectively. The magnitude contours in Fig. 10a are in anti-phase with those in Fig. 10b, which means that the oscillation period of the $S_{\mathrm{QSM},1}$ term is a half of the vortex shedding period. Fig. 10c–f shows the distribution of the $S_{\mathrm{QSM},2}$ term of Eq. (12) at approximately $0.0T_{\mathrm{a}}$, $0.25T_{\mathrm{a}}$, $0.5T_{\mathrm{a}}$ and $0.75T_{\mathrm{a}}$, respectively. The oscillation period of the $S_{\mathrm{QSM},2}$ term is the same as the vortex shedding cycle. From this, it can be found that the period of oscillation of the self-noise sources in the streamwise direction is approximately half of that in the direction perpendicular to the streamwise direction. From the flow simulation result in Fig. 5, it was shown that the oscillation frequency in drag is twice the Strouhal number corresponding to the lift fluctuation. Thus it is evident that the drag dipole source associated with the drag force varies twice as the frequency of the lift dipole source associated with the lift force. This frequency characteristic of the self-noise source is noted here for future reference in the following section. Furthermore, the fluctuating magnitude of the $S_{\mathrm{QSM},1}$ term in the streamwise direction is two times larger than that in the direction normal to the streamwise direction.

4.3. *Acoustic field prediction*

Acoustic calculations were first performed with the modelled source term from the approximated Lighthill's stress source term S_{ALST} of Eq. (5), as discussed in Section 4.2. Fig. 11a–d shows contours of the instantaneous pressure over the whole computation domain at approximately one quarter of a cycle, a half cycle, three quarters of a cycle and the beginning of a cycle, respectively. The acoustic field directivity is seen to have a dipole pattern, whose axis is approximately in the direction normal to the free stream velocity. This behavior reveals the physical origin of the dipolar sound of the aeolian tone radiation as being due to a scattering mechanism whereby the shear motion of vorticity waves are converted into acoustical energy at the solid wall of the cylinder.

The pressure contours, shown in Fig. 11, are the result of using the approximated Lighthill's stress tensor to model

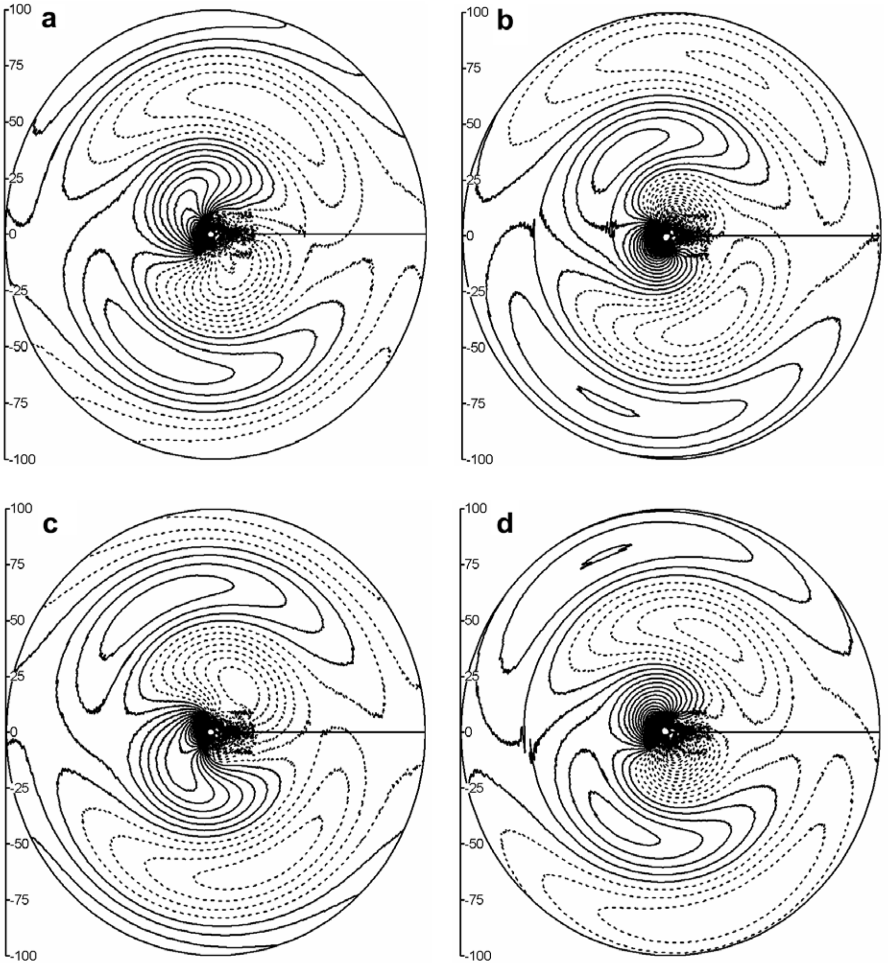

Fig. 11. Iso-contours of the fluctuating pressure over the whole computation domain by using the approximated Lighthill's stress tensor of Eq. (5) during one period (with 150 levels from −3.17e−3 to 1.44e−3): (a) $t_{\mathrm{a}} = 250$, (b) $t_{\mathrm{a}} = 270$, (c) $t_{\mathrm{a}} = 290$ and (d) $t_{\mathrm{a}} = 310$.

the source term. Note that S_{ALST} of Eq. (5) includes the non-oscillating part $S_{0,i}$ of Eq. (11). The prediction in Fig. 11 therefore includes the background mean pressure, which is why the positive pressure pulses propagate upstream whereas the negative pressure pulses propagate downstream. A similar phenomenon was also reported by Inoue and Hatakeyama [12]. In order to isolate the fluctuating part of the propagating acoustic pressure, the acoustic simulation was repeated with the source terms now defined as $S'_{\mathrm{ALST},i} = \rho_0 \partial u_i u_j / \partial x_j - \overline{\rho_0 \partial u_i u_j / \partial x_j}$, i.e., with the mean part removed.

The results predicted from the use of this new source term are shown in Fig. 12. These figures show that both positive and negative pulses appear to propagate in the direction almost normal to the mean flow direction. Thus, by comparing Figs. 11 and 12, it appears that the propagation angles of the total pressure and the fluctuation pressure differ. However, this cannot be correct because, as indicated by Inoue and Hatakeyama [12], the difference between the total pressure and the fluctuating pressure is the mean pressure which does not contain temporal information.

Fig. 13 shows the pressure waveform along the x_2-axis ($x_2 > 0$) at various instants in time. The dashed line is directly proportional to $x_2^{-0.5}$ and can be seen to correspond to the envelope of the pressure distribution along the x_2-axis, as is characteristic of the cylindrical decay of two-dimensional sound fields.

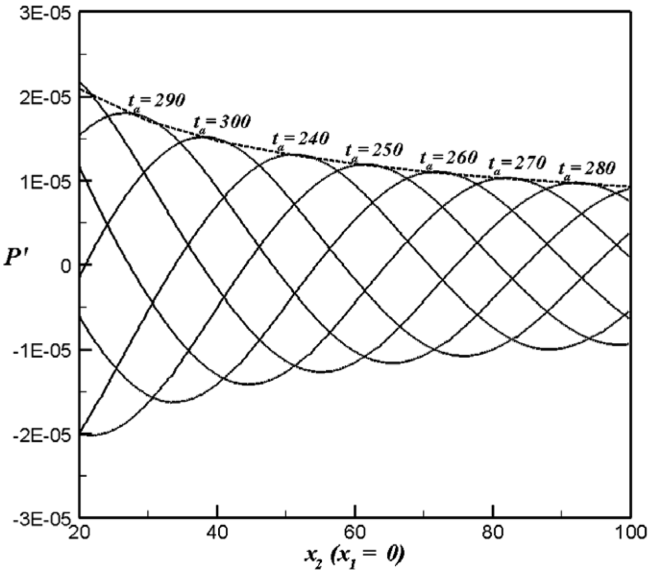

Fig. 13. Instantaneous pressure waveforms along the x_2-axis ($x_2 > 0$) : —, numerical results, - - -, line corresponding to $a/x_2^{0.5}$ where a is the value of pressure at $x_2 = 92.5$ in the line of $t_a = 280$.

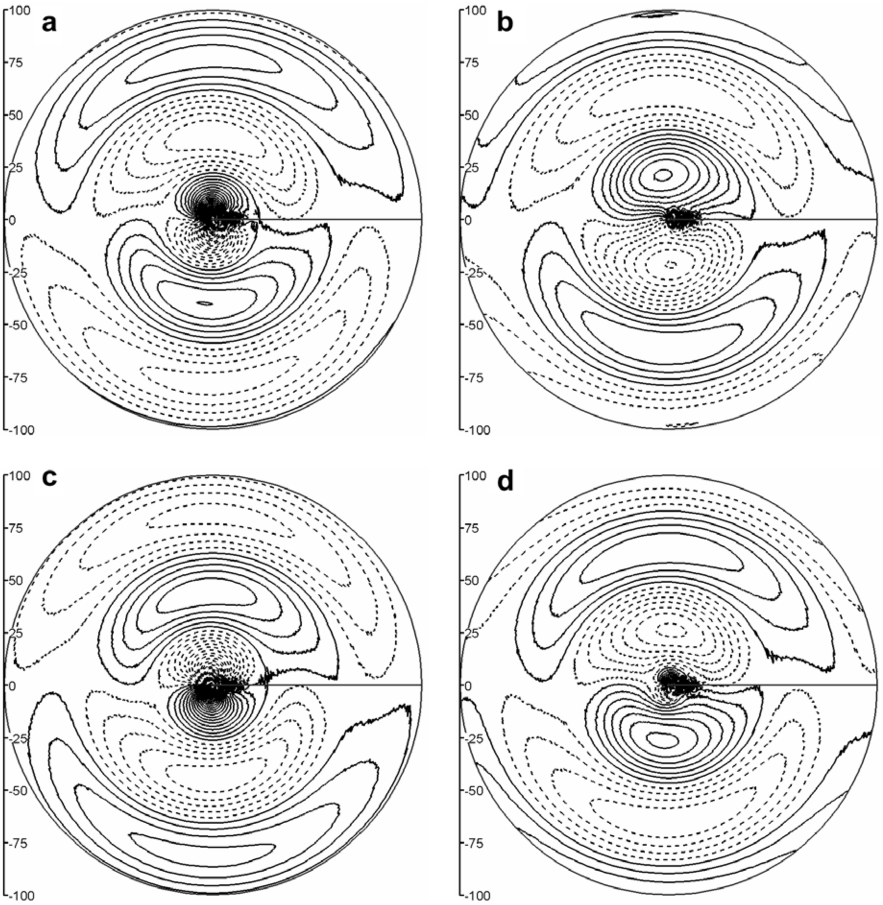

Fig. 12. Iso-contours of the fluctuating pressure over the whole computation domain by using the source $S'_{\mathrm{ALST},i} = S_{\mathrm{ALST},i} - \overline{S_{\mathrm{ALST},i}}$ during one period (with 150 levels from −2e−4 to 2e−4): (a) $t_a = 230$, (b) $t_a = 250$, (c) $t_a = 270$ and (d) $t_a = 290$.

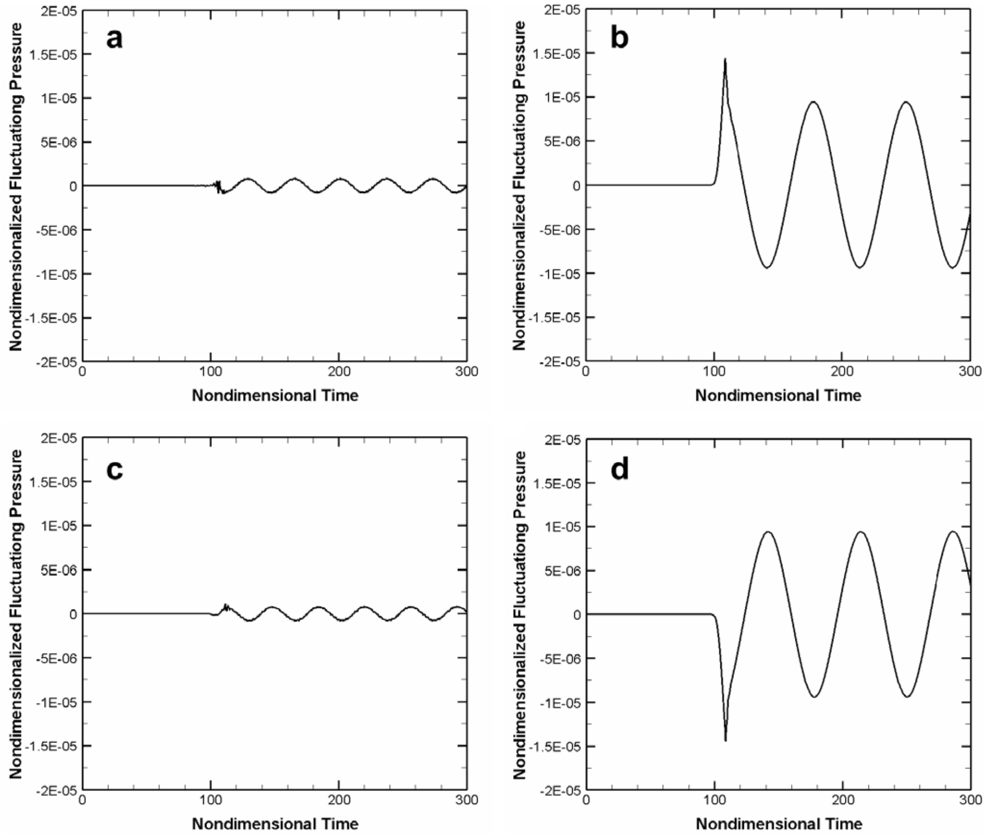

Fig. 14. Fluctuating pressure signal at $r = 99D$ measured at (a) $\theta = 0°$, (b) $\theta = 90°$, (c) $\theta = 180°$, and (d) $\theta = 270°$. (The angles are measured from the x-axis in counter-clock wise direction.)

The time history of the fluctuating pressure, predicted at a distance $r = 99D$ from the cylinder center, is shown in Fig. 14 at the four angular positions of $\theta = 0°$, 90°, 180° and 270°, which denote the angles from the x_1-axis in a counter-clock wise direction. The time signals pass through a transient state to arrive at a state of steady periodicity. It is observed that the pressure signals at $\theta = 90°$ and 270° are dominated by signals oscillating at the Strouhal frequency, and the signals at 0° and 180° by signals oscillating at twice the Strouhal frequency. This is a physically plausible result because the lift dipole is dominant at the Strouhal frequency and the drag dipole is dominant at twice the Strouhal frequency.

The directivity pattern of the sound field in the current example, computed at a distance $r = 99D$ from the cylinder center, is shown in Fig. 15. Numerical results are compared with the analytic solution described in detail in Appendix for the sound radiation due to a compact source in an uniform flow. The directivity obtained using the fine grid (201×1998 grid points, i.e., $\Delta\theta_{\min} = 0.0157$ and $\Delta r = 0.05$) shows good agreement with the magnitude of the directivity at 90° and 180°, being just 6% less than that predicted by the analytic solution. The difference between the numerical and analytic solution can be attributed to the absence of viscous stress source terms in the Lighthill's stress tensor. The current method is equivalent to that obtained using the Green function solution of Lighthill's equation with the Green function chosen to satisfy the hard-walled boundary condition on the cylinder surface. Recently, Pérot et al. [29] calculated aeolian tone noise by using a tailored Green's function to solve Lighthill's equations. They also showed that the results conform to

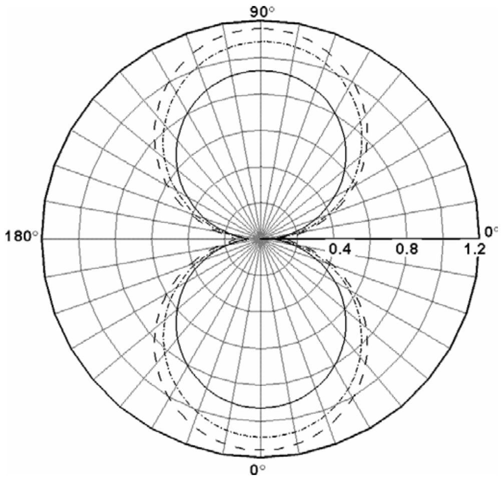

Fig. 15. Directivity patterns of the rms value of the fluctuating pressure at $r = 99D$: --- analytic results, -·-·- using S_{ALST} with 201×1998 grids, — using S_{ALST} with 101×998 grid.

those obtained by using Curle's acoustic analogy [4]. However, their result differs by 10% from the solution obtained using Curle's acoustic analogy.

The numerical results obtained using the relatively coarse mesh (101×998 grid points, i.e., $\Delta\theta_{\min} = 0.0314$ and $\Delta r = 0.1$) show relatively larger differences compared with that obtained from the analytic solution. However, assuming that the relative levels of the far field radiation obtained using each sub-source of the approximated Lighthill's stress tensor is the same using the fine mesh and the coarse mesh, all of the following calculations are performed using the 101×998 grid in order to reduce computation time.

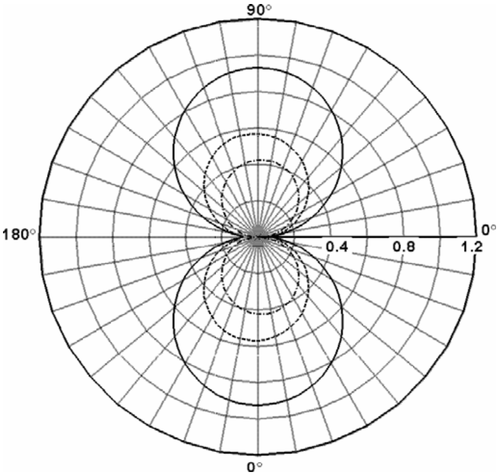

Fig. 16. Directivity patterns of the rms value of the fluctuating pressure at $r = 99D$: — using both of the $S_{\mathrm{ALST},1}$ and $S_{\mathrm{ALST},2}$ terms of Eq. (5), - - - using only $S_{\mathrm{ALST},1}$ without $S_{\mathrm{ALST},2}$ and -·-·- using only $S_{\mathrm{ALST},2}$ without $S_{\mathrm{ALST},1}$.

It is well documented [4,5,12] that the lift-dipole source is the dominant contribution to the overall radiation produced by a circular cylinder in a cross-flow. In order to investigate the sound generation mechanism of aeolian tones in greater detail, the approximated Lighthill stress tensor is divided into its x_1(drag)-components and x_2(lift)-components, i.e., the source terms of $S_{\mathrm{ALST},1}$ and $S_{\mathrm{ALST},2}$ of Eq. (5). Acoustic computations are then performed with only one source component present, i.e., with $S_{\mathrm{ALST},1}$ present but not $S_{\mathrm{ALST},2}$ and vice versa. The predicted directivities of the fluctuating pressure at $r = 99D$ for the two cases and that with both source terms present are shown in Fig. 16.

The contributions of the two source components to total aeolian tone noise are found to be comparable. However, the directivity obtained by using the $S_{\mathrm{ALST},1}$ term is slightly larger than that obtained by using the $S_{\mathrm{ALST},2}$ source term. This appears contrary to the fact that the lift dipole in the x_2-direction is dominant in aeolian tone noise generation. This anomaly seems to be due to the geometry of the cylinder. According to Curle's acoustic analogy, aeolian tone noise from a circular cylinder can be expressed in terms of unsteady forces over the surface of the cylinder. Neglecting viscous stresses on the cylinder surface, the unsteady force can be expressed entirely in terms of the unsteady pressure on the cylinder surface. Assuming that the source region is compact and that the flow is isentropic, aeolian tone levels in the far-field can be predicted using the lift and drag forces which are directly connected to the

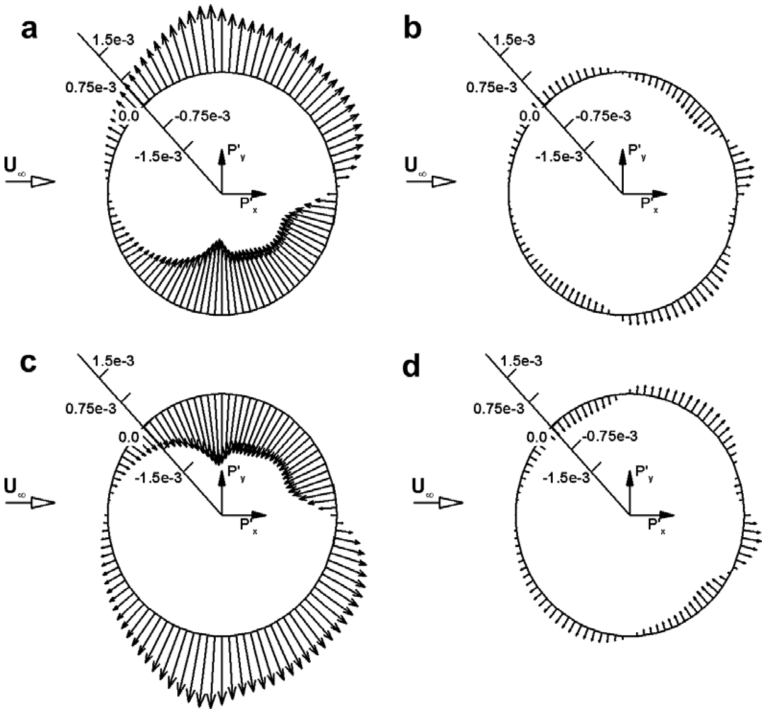

Fig. 17. A snapshot of the fluctuating hydrodynamic pressure ($P' = P - p_0$) on the cylinder surface at (a) one quarter of a cycle, (b) a half cycle, (c) three quarters of a cycle, (d) the beginning of a cycle.

unsteady pressure distribution around the cylinder surface. The ratio of the contribution from the unsteady pressure to the lift and dipole forces depends on the distribution of the unsteady pressure on the cylinder surface. Pressure fluctuations on the cylinder surface within the range of angles of 45° to 135° and 225° to 315° (see Fig. 15 or Fig. 16 for the angle notation) makes the greatest contribution to the lift force, while those outside of this range of angles make most contribution to the drag force. The large fluctuating magnitudes of the $S_{\mathrm{ALST},1}$ and $S_{\mathrm{ALST},2}$ sources around the cylinder surface in Fig. 7 lead to the large hydrodynamic pressure fluctuations over the cylinder surface.

Fig. 17 shows a snapshot of the fluctuating hydrodynamic pressure on the cylinder surface at four instants in time over a vortex shedding period. It is seen that the most intense fluctuations of the hydrodynamic pressure on the cylinder surface occur within the angle range of 45–100° and 260–315°, of which the distribution is essentially related to the distribution of the S_{ALST} around the cylinder surface. Therefore, the fluctuation of the lift force of the cylinder is more intense (approximately 10-times larger in this computation) than that of the drag force. This difference suggests that the lift-dipole sources are more important to aeolian tone noise generation than the drag-dipole source.

The use of Eq. (8) allows a more detailed investigation into the mechanism of aeolian tone generation by decomposing the approximated Lighthill's stress tensor into the shear- and self-noise source components of $S_{\mathrm{shear},i}$ and $S_{\mathrm{self},i}$. The term $S_{\mathrm{shear},i}$ of Eq. (10) represents the interaction term between the mean and fluctuating components of the flow, while the term $S_{\mathrm{self},i}$ of Eq. (9) represents the interaction between the fluctuating quantities and is equivalent to the QSM of Eq. (12). Fig. 18 shows the instantaneous pressure contours obtained using only (a) the shear-noise sources and (b) the self-noise sources. The resultant directivity of rms pressure directivity is shown in Fig. 18c. Unlike free sheared flows, where the self-noise sources are known to play a dominant role in the noise generation mechanism, the shear-noise sources make the largest contribution to the total aeolian tone noise. Contributions by the self-noise sources are negligible. In addition, the acoustic field due to the self-noise sources is substantially different from that due to the shear-noise sources. The acoustic field due to the shear-noise sources has a directivity similar to that of

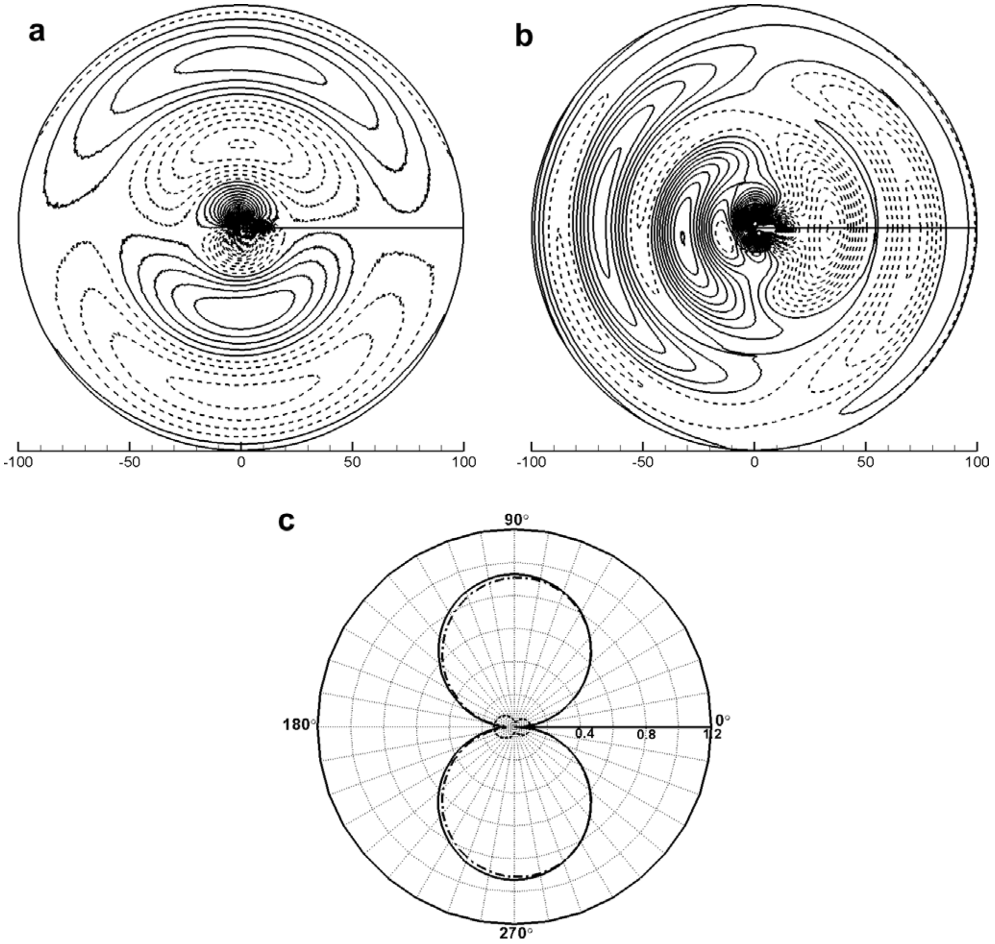

Fig. 18. Instantaneous pressure contours over the whole computation domain by (a) using the $S_{\mathrm{shear},i}$ term (with 150 levels from −2e−4 to 2e−4) and (b) using the $S_{\mathrm{self},i}$ term (with 100 levels from −2e−5 to 2e−5), and (c) directivity patterns of the rms value of the fluctuating pressure at $r = 99D$: — by using the $S_{\mathrm{ALST},i}$, -·-·- by using the $S_{\mathrm{shear},i}$ and --- by using the $S_{\mathrm{self},i}$.

the lift dipole, while the acoustic field due to the self-noise sources has a directivity similar to that of the drag dipole source, whose dominant frequency is identical to that of the self-noise sources in the x_1-direction, as mentioned previously. The largest variation of the self-noise source in Fig. 10 is located within the angle-range of −50° to 50°. The self-noise source therefore makes most contribution to the sound field due to the drag dipole source.

5. Conclusion

Aeolian tone noise generation by a two-dimensional circular cylinder in a uniform cross-flow is investigated. Hybrid CAA methods are utilized to compute the modelled source terms and their acoustic fields. Numerical results obtained using the acoustic solver, together with the approximated Lighthill's stress tensor to represent the source terms, are shown to be in good agreement with those computed from dipole sources obtained using Curle's solution to the acoustic analogy. This paper has found that the approximated Lighthill stress source term in the flow-direction makes a contribution to overall aeolian tone noise that is comparable with the component in the direction normal to the mean flow. It is also shown that shear-noise sources make the greatest contribution overall, and that the self-noise sources are generally negligible. From these findings, it may be inferred that the noise generation mechanism in wall-bounded sheared flows is fundamentally different from that in free sheared flows, where the self-noise sources dominate the shear-noise sources.

Acknowledgement

This work was supported by Pusan National University Research Grant, 2006.

Appendix. Analytic solution for 2-D point dipole

The results of the present method are verified by comparison with the analytic solution [30] of the two-dimensional, far-field sound radiated by a two-dimensional dipole source situated in a smooth flow. These can be derived by assuming a harmonic time dependence, and by using the closed form solution to the Helmholtz equation. The following approximations are made:

- The source is a point dipole.
- Very low frequency $k_0D \ll 1$ where D is the diameter of the cylinder (the present case $k_0D = 0.08595$ and 0.17190 for the lift and drag dipole source variations, respectively).

The sound field due to a two-dimensional compact rigid body situated in a smooth flow may be approximated by a point dipole source. The radiated rms acoustic pressure radiated from the point dipole source is directly proportional to the rms fluctuating force per unit length on the cylinder surface, so that

$$p_{\mathrm{rms}}(r,\theta) = \frac{1}{2}\sqrt{\frac{\omega}{2\pi r c_\infty}} F_{\mathrm{rms}} \sin\theta. \tag{A.1}$$

The fluctuating forces per unit length comprise two-dimensional lift and drag components. Eq. (A.1) does not include the effects of the volume-quadrupole sources, and is therefore applicable to low Mach number flows. The rms acoustic pressure can be written in the form

$$p_{\mathrm{rms}}(R,\theta) = \frac{\rho_\infty u_\infty^2 D}{4}\sqrt{\frac{\omega}{2\pi c_\infty R}}[C_{\mathrm{l,rms}}\cos\theta + 4C_{\mathrm{d,rms}}\sin\theta], \tag{A.2}$$

where ω is the angular frequency, R is the distance from the source point to the observer and $C_{\mathrm{l,rms}}$ and $C_{\mathrm{d,rms}}$ are the rms vales of the fluctuating lift and drag coefficients determined from the viscous simulation. The angular frequency is determined using the Strouhal number of the vortex shedding from a circular cylinder in the viscous flow simulation.

References

[1] Lighthill MJ. On sound generated aerodynamically – I. General theory. Proc Royal Soc Ser A 1952;211:564–87.

[2] Curle N. The influence of solid boundaries upon aerodynamic sound. Proc Royal Soc Ser A 1955;231:505–14.

[3] Ffowcs Williams JE, Hawkings JE. Sound generation by turbulence and surfaces in arbitrary motion. Philo Trans R Soc London Ser A 1968;264:321–42.

[4] Hardin JC, Lamkin SL. Aeroacoustic computation of cylinder wake flow. AIAA J 1984;22:51–7.

[5] Cox JS, Brentlner KS, Rumsey CL. Computation of vortex shedding and radiated sound for a circular cylinder: subcritical to transonic Reynolds numbers. Theor Comput Fluid Dyn 1988;12:233–53.

[6] Hardin JC, Pope DS. An acoustic/viscous splitting technique for computational aeroacoustics. Theor Comput Fluid Dyn 1994;6: 323–40.

[7] Hardin JC, Pope DS. Sound generation by flow over a two-dimensional cavity. AIAA J 1995;33:407–12.

[8] Shen WZ, Sørensen JN. Comment on the aeroacoustic formulation of Hardin and Pope. AIAA J 1999;37:141–3.

[9] Shen WZ, Sørensen JN. Aeroacoustic formulation of low-speed flows. Theor Comput Fluid Dyn 1999;13:271–89.

[10] Shen WZ, Sørensen JN. Aeroacoustic modeling of turbulent airfoil flow. AIAA J 2001;39:1057–64.

[11] Ewert R, Schröder W. Acoustic perturbation equations based on flow decomposition via source filtering. J Comput Phys 2003;188:365–98.

[12] Inoue O, Hatakeyam H. Sound generation by a two-dimensional circular cylinder in a uniform flow. J Fluid Mech 2002;471:285–314.

[13] Dowling AP, Ffowcs-Williams JE. Sound and sources of sound. London, England: Ellis Horwood Limited; 1983 [p. 15 in Chapter 1].

[14] Ryu J, Cheong C, Kim S, Lee S. Computation of internal aerodynamic noise from quick-opening throttle valve using frequency-domain acoustic analogy. Appl Acoust 2005;66:1278–308. doi:10.1016/j.apacoust.2005.04.002.

[15] Bogey C, Bailly C, Juve D. Computation of flow noise using source terms in linearized Euler's equations. AIAA J 2002;40: 235–43.

[16] Chien KY. Prediction of channel and boundary layer flows with a low Reynolds number turbulence model. AIAA J 1982;20: 33–8.

[17] Cheong C, Lee S. Grid-optimized dispersion-relation-preserving schemes on general geometries for computational aeroacoustics. J Comput Phys 2001;174:248–76. doi:10.1006/jcph.2001.6904.

[18] Tam CKW, Web JC. Dispersion-relation-preserving schemes for computational acoustics. J Comput Phys 1993;107:262–81.

[19] Hu FQ, Hussaini MY, Manthey JL. Low-dissipation and low-dispersion Runge–Kutta schemes for computational aeroacoustics. J Comput Phys 1996;124:177–91.

[20] Bayliss A, Turkel E. Far field boundary conditions for compressible flow. J Comput Phys 1982;48:182–99.

[21] Tam CKW, Dong Z. Wall boundary conditions for high-order finite difference schemes for computational aeroacoustics. Theor Comput Fluid Dyn 1994;8:303–22.

[22] Tam CKW, Shen H. Direct computation on nonlinear acoustic pulses using high-order finite difference schemes. AIAA paper 93-4325, 1993.

[23] Kang DJ, Bae SS, Joo SW. An unstructured FVM for the numerical prediction of incompressible viscous flows. Trans KSME 1998;22:1410–21.

[24] Kang DJ, Bae SS. Navier–Stokes simulation of MIT FFX ffx by using an unstructured finite volume method. ASME Turbo-Expo IGTI-99-214, 1999.

[25] Thomadakis M, Leschziner M. A pressure correction method for the solution of incompressible viscous flows on unstructured grids. Int J Numer Methods Fluids 1996;22:581–600.

[26] Hobson GV, Lakshiminarayana B. Prediction of cascade performance using an incompressible Navier–Stokes technique. J Turbomach 1991;113:561–72.

[27] Kiya M, Arie M, Tamura H, Mori H. Vortex shedding from two circular cylinders in staggered arrangement. Trans ASME 1980;102:166–73.

[28] Cantwell B, Coles C. An experimental study of entrainment and transport in the turbulent near wake of a circular cylinder. J Fluid Mech 1983;136:321–74.

[29] Perot F, et al. Numerical prediction of the noise radiated by a cylinder. AIAA Paper 2003-3204, 2003.

[30] Blake WK. Mechanics of flow-induced sound and vibration, vol. 1. Academic Press, Inc.; 1986. p. 280–283.